RESEARCH

Viscous and thermal velocity slip coefficients via the linearized Boltzmann equation with ab initio potential

Thanasis Basdanis[1] · Dimitris Valougeorgis[1] · Felix Sharipov[2]

Abstract

The viscous and thermal velocity slip coefficients of various monatomic gases are computed via the linearized classical Boltzmann equation, with ab initio potential, subject to Maxwell and Cercignani–Lampis boundary conditions. Both classical and quantum interatomic interactions are considered. Comparisons with hard sphere and Lennard–Jones potentials, as well as the linearized Shakhov model are performed. The produced database is dense, covers the whole range of the accommodation coefficients and is of high accuracy. Using symbolic regression, very accurate closed form expressions of the slip coefficients, easily implemented in the future computational and experimental works, are deduced. The thermal slip coefficient depends, much more than the viscous one, on the intermolecular potential. For example, in the case of diffuse scattering, the relative differences in the viscous slip coefficient data between HS and AI potentials are less than 4%, whilst the corresponding ones in the thermal slip coefficient data are about 6% for He, reaching 15% for Xe. Quantum effects are considered for He, at temperatures 1–10^4 K to deduce that deviations from the classical behaviour are not important in the viscous slip coefficient, but they become important in the thermal slip coefficient, where the differences between the classical and quantum approaches reach 15% at 1 K. The computational effort of solving the linearized Boltzmann equation with ab initio and Lennard–Jones potentials is the same. Since ab initio potentials do not contain any adjustable parameters, it is recommended to use them at any temperature.

1 Introduction

The computation of the viscous slip coefficient (VSC) and the thermal slip coefficient (TSC) of velocity, via kinetic theory, are problems of fundamental importance in rarefied gas dynamics (Sharipov 2016). These coefficients are employed in the velocity slip boundary conditions, which are widely used, under moderate gas rarefaction

conditions, in order to extend the range of validity of the applied continuous-type fluid-dynamics model. This way, the correct macroscopic fluid behaviour is recovered, whilst the computational expensive solution of mesoscale kinetic-type models in the slip and early transition regimes is circumvented. Such approaches belong to the field of extended hydrodynamics and are implemented in numerous engineering and technological fields including gaseous microfluidics (Kandlikar and Garimella 2006; Colin 2014; Veijola et al. 2010), vacuum gas technology and pumping (Pearce et al. 2013; Jousten and Jousten 2016; Vasileiadis et al. 2016), metrology (Naris et al. 2018; Verbovsek et al. 2019), lubrication (Breuer 2002), porous media (Moghaddam and Jamiolahmady 2016; Johansson et al. 2019; Zhang et al. 2022) and high-altitude gas dynamics (Le et al. 2012). Furthermore, the velocity slip boundary conditions are commonly employed in the estimation of the accommodation coefficients, characterising gas–surface interaction, by accordingly matching computational

✉ Thanasis Basdanis
  abasdanis@mie.uth.gr

  Dimitris Valougeorgis
  diva@mie.uth.gr

  Felix Sharipov
  sharipov@fisica.ufpr.br

[1] Department of Mechanical Engineering, University of Thessaly, Volos, Greece

[2] Department of Physics, Federal University of Parana, Curitiba, Brazil

and experimental results (Silva et al. 2016; Yamaguchi et al. 2016; Wu and Struchtrup 2017). Therefore, in many aspects, the VSC and the TSC have the same importance with the transport coefficients and, as in the latter case, their theoretical computation is achieved only via kinetic theory. They may be computed in a direct manner by solving the corresponding classical half-space problems or alternatively, in an indirect manner by solving the associated slab geometry problem (Poiseuille or Couette flow for the VSC and thermal creep flow for the TSC) in the slip regime (Sharipov 2016; Ivchenko et al. 2007). In the latter case, the computed kinetic flow rate or shear stress is compared to the corresponding one obtained by the Stokes equation with slip boundary conditions to deduce the coefficient.

Due to their importance, VSC and TSC have been extensively investigated. A recent and detailed review on the topic, with all available data of the slip coefficients, obtained with various kinetic equations and computational methods, is provided in Sharipov (2011). Therefore, our introductory discussion here is brief and closely related to the scope of the present work. The involved kinetic equations mainly include the linearized BGK and the Shakhov (S) kinetic models, as well as the linearized Boltzmann equation (LBE), which are numerically solved based on various versions of variational methods, moment methods and discrete ordinates or velocity methods. Most of the available data on the slip coefficients are via the kinetic model equations, subject to purely diffuse boundary conditions (DBC), Maxwell boundary conditions (MBC) and Cercignani–Lampis boundary conditions (CLB) (a long list of cited works is included in Sharipov (2011)). Some data are also available via the LBE with hard sphere (HS) potential for DBC (Sone et al. 1989; Cercignani and Lorenzani 2010), MBC (Loyalka and Hickey 1990; Siewert 2003a; Gibelli 2012) and CLB (Siewert 2003b; Garcia and Siewert 2010; Nguyen et al. 2020). Corresponding data with other potentials are very limited. There are two studies with Lennard–Jones (LJ) intermolecular potential at temperatures around 300 K and purely diffuse reflection (Sharipov 2011; Loyalka 1990) and another, very recent one, focussed on the TSC with variable hard sphere potential and CLB (Wang et al. 2020). The major findings on the velocity slip coefficients may be summarised as follows (Sharipov 2011):

- The VSC, denoted by σ_P, depends very weakly on the employed kinetic equation and the potential. In the case of the LJ potential the reported VSC is about the same for all monatomic gases. For purely diffuse scattering, the VSC varies as $0.968 \leq \sigma_P \leq 1.03$ (recommended value for engineering purposes $\sigma_P = 1$). Furthermore, σ_P depends strongly on the accommodation coefficient $0 \leq \alpha_M \leq 1$ of the MBC, whilst in the case of CLB, it strongly depends on the tangential momentum accom-

modation coefficient $0 \leq \alpha_t \leq 2$, but it is almost independent of the normal kinetic energy accommodation coefficient $0 \leq \alpha_n \leq 1$.

- The TSC, denoted by σ_T, depends, much more than the VSC, on the employed kinetic equation and intermolecular potential. The reported data with diffuse reflection vary as $1.018 \leq \sigma_T \leq 1.18$ (recommended value for engineering purposes $\sigma_T = 1.1$). Also, the TSC depends strongly on the gas–surface interaction kernel and the involved accommodation coefficients, i.e. on α_M of the MBC and on both (α_t, α_n) of the CLB. Taking into consideration all above (strong dependency on the employed kinetic equation, potential and boundary conditions), as well as the limited available data with the LBE and the observed discrepancies between computational and experimental results in thermal creep flows (Silva et al. 2016; Yamaguchi et al. 2016; Basdanis et al. 2022), it is necessary to obtain additional TSC data, via the LBE, with LJ or other realistic intermolecular potential, subject to physically justified boundary conditions (e.g. CLB).

Intermolecular potentials are vital in kinetic theory and detailed information may be found in many kinetic theory and rarefied gas dynamics books [e.g. (Ivchenko et al. 2007; Ferziger and Kaper 1972; Shen 2005)]. Surely, the HS model is the simplest and most widely used potential. As it is well known however, this model neglects the attractive intermolecular force and provides the viscosity and thermal conductivity transport coefficients proportional to the square root of temperature and therefore, it may lead to erroneous prediction of transport phenomena. To remedy the inefficiencies of the HS model, other more advanced models, such as the inverse power law, the Sutherland, the Lennard–Jones and the Stockmayer potentials, which rely, at certain extent, on physical reasonings of intermolecular collisions, have been proposed. Certainly, the computational effort of solving the LBE with these complex potentials is significantly increased and therefore, only few studies, related to classical one-dimensional flows, have been reported (Loyalka 1990; Wang et al. 2020; Sharipov and Bertoldo 2009a, b; Wu et al. 2015). Alternatively, there are several potential models specifically elaborated mainly for the direct simulation Monte Carlo (DSMC) method (Bird 1994). These models include the widely used variable hard sphere model, as well as the variable soft sphere and the generalised hard and soft-sphere models (Shen 2005). In all these collision models, the sampling of the distribution of the post-collision velocity direction is kept simple and the computational DSMC effort remains modest. Also, the methodology proposed in Sharipov and Strapasson (2012a), based on lookup tables of the differential cross section, allows the computationally efficient implementation of any potential in the DSMC method.

All aforementioned phenomenological potentials however, have the following common drawback: they all rely on one or more adjustable parameters, which are extracted from many kinds of experimental data and are valid only in narrow temperature ranges and therefore, may not accurately recover the transport coefficients at extremely low and high temperatures. On the contrary, ab initio (AI) potentials, which are available in the literature for all noble gases and their mixtures (Cybulski and Toczyłowski 1999; Przybytek et al. 2010; Cencek et al. 2012; Hellmann et al. 2008, 2017; Patkowski and Szalewicz 2010; Jäger et al. 2009, 2016; Jäger and Bich 2017; Haley and Cybulski 2003), are based on first principals and do not contain any adjustable parameters. More importantly, following (Sharipov and Strapasson 2012a), a computationally efficient methodology of applying AI potentials in the DSMC method has been elaborated and validated in a series of benchmark studies, focussing on the computation of the transport coefficients and the solution of the Couette and Fourier flows for single gases and gas mixtures (Sharipov and Strapasson 2012b, 2013; Strapasson and Sharipov 2014; Sharipov 2022). More recently, the same methodology has been used to introduce AI potential with quantum scattering in DSMC calculations in order to consider quantum effects in light gases at low temperatures (Sharipov 2018a, b; Sharipov and Dias 2019; Zhu et al. 2019). By simulating the Couette and Fourier flows, it has been found that quantum effects are non-negligible at temperatures less than 300 K in single gases and 500 K in gas mixtures, whilst they become significant at temperatures less than 50 K. Rarefied gas flows at low temperatures appear in several technological applications (e.g. vacuum sciences (Mozetič et al. 2014), cryogenic systems and processes in fusion reactors (Kalinin et al. 2006; Tantos et al. 2016; Pearce et al. 2012; Zhang and Miller 2016), cryogenic separation/capture of gases (Hart and Gnanendran 2009; Oh and Hirscher 2016) and high temperature superconducting power devices (Graber et al. 2015; Cheetham et al. 2016)).

Based on all above, in the present work, VSC and TSC are computed based on the classical LBE with AI potential, subject to DBC, MBC and CLB for five monatomic gases, namely He, Ne, Ar, Kr and Xe. The spatial evolution of the distribution function is always classical, whilst quantum scattering is considered in the binary intermolecular interaction (Ferziger and Kaper 1972). In the case of He, both classical and quantum scattering are considered at temperatures ranging from 1 K up to 10^4 K, in order to evaluate the quantum effects. The coefficients are computed via the half-space problems, as well as the associated slab geometry ones for benchmarking purposes. The deduced data are dense in terms of the involved accommodation coefficients and may be considered of high fidelity since they are based on the LBE and AI potential. Furthermore, since this is the first time that the AI potential is used in the LBE, the additional computational effort, compared to the HS and LJ potentials, is examined.

2 Formulation

For both coefficients under investigation, a semi-infinite expanse of a monoatomic gas in the half-space $x' > 0$, bounded by a planar infinite plate at $x' = 0$, is considered. The characteristic length is the equivalent free path $l_0 = \mu' v_0 / P_0$, where μ' is the viscosity and $v_0 = \sqrt{2kT_0/m}$ is the most probable speed, with k_B denoting the Boltzmann constant, m the molecular mass, T_0 a reference temperature and P_0 is some reference pressure. Henceforth, $x = x'/l_0 \in [0, \infty)$ denotes the dimensionless distance from the wall and $\mathbf{c} = \boldsymbol{v}/v_0 = (c_x, c_y, c_z)$ is the dimensionless molecular velocity.

The governing equation is the LBE, which in dimensionless form, is written as (Ivchenko et al. 2007; Sharipov and Bertoldo 2009a, 2009b)

$$c_x \frac{\partial h_i(x, c_x, c_y, c_z)}{\partial x} = 2\mu L(h_i) + s_i(c_x, c_y, c_z). \tag{1}$$

Here, the subscript $i = $ VS, TS corresponds to VSC and TSC problems respectively, $h_i(x, c_x, c_y, c_z)$ is the corresponding unknown perturbed distribution function, $L(h_i)$ is the linearized collision operator and $\mu = (\mu' d^2)/(m v_0)$ is the dimensionless viscosity, with d denoting a characteristic atomic size (the zero point of the AI potential, given in Table 13 of Appendix 1 and the molecular diameter for HS potential).

It is noted that Eq. (1) is the classical Boltzmann equation, which is valid for a dilute monoatomic gas, subject to binary collisions, with the well-known assumption that the molecules involved in a collision are uncorrelated. The spatial evolution of the perturbed distribution function is classical, whilst quantum effects are considered only in the binary intermolecular interaction via quantum scattering. This assumption is valid under the condition $(n\hbar^3)/(2\pi m k_B T)^{3/2} << 1$, see Eq. (9.3–1) in Ferziger and Kaper (1972), which is fulfilled at all temperatures T, considered here, provided that the number density n is adequately small ($\hbar$ is the Planck constant and k_B is the Boltzmann constant). Equation (1) may be considered as a classical limit of the quantum Boltzmann equation of the form provided by Uehling–Uhlenbeck, see Eq. (10.1–5) in Hirschfelder et al. (1954).

Also, it may be useful to note that the range of applicability of the BE based on AI potential is the same as for any other potential and is determined by the assumptions used to derive the BE. For instance, the applicability of the BE based on AI for helium is analysed in Cencek et al. (2012), where the

transport and the virial coefficients are calculated in the temperature range from 1 to 10,000 K. At any given temperature, these results are valid for any pressure lower than the corresponding pressure of saturated vapour.

Each coefficient is computed with the corresponding source term $s_i(c_x, c_y, c_z)$, driving the flow as follows:

- Viscous slip: $s_{VS}(c_x, c_y, c_z) = -2c_x c_y$.
- Thermal slip: $s_{TS}(c_x, c_y, c_z) = -c_y\left(c^2 - \frac{5}{2}\right)$.

The number of the molecular velocity components may be reduced by introducing, in the molecular velocity space, the cylindrical coordinates $\mathbf{c} = (c_x, c_r, \theta)$, with $c_r = \sqrt{c_y^2 + c_z^2}$ and $\theta = \tan^{-1}(c_z/c_y)$. The unknown distributions are expressed as

$$h_i(x, c_x, c_y, c_z) = Y_i(x, c_x, c_r)\cos\theta, \ i = \text{VS, TS}, \quad (2)$$

and then, the dimensionless LBE is written as

$$c_x \frac{\partial Y_i(x, c_x, c_r)}{\partial x} = 2\mu L(Y_i) + s_i(c_x, c_r), \ i = \text{VS, TS}, \quad (3)$$

where the main unknowns are the distribution functions $Y_i(x, c_x, c_r)$. The source terms are:

$$s_{VS}(c_x, c_r) = -2c_x c_r, \ s_{TS}(c_x, c_r) = -c_r(c^2 - 5/2). \quad (4)$$

The linearized collision term $L(Y_i)$ reads

$$L(Y_i) = \frac{1}{\pi^{3/2}} \int\limits_{-\infty}^{+\infty}\int\limits_{0}^{+\infty} \tilde{K}(c_x, c_r, \hat{c}_x, \hat{c}_r)$$
$$\left[Y_i(x, \hat{c}_x, \hat{c}_r) - \frac{\Psi_i(\hat{\mathbf{c}})}{\Psi_i(\mathbf{c})} Y_i(x, c_x, c_r) \right] \exp\left(-\hat{c}^2\right)\hat{c}_r \mathrm{d}\hat{c}_r \mathrm{d}\hat{c}_x, \quad (5)$$

where $\mathbf{c} = (c_x, c_r, \theta)$ and $\hat{\mathbf{c}} = (\hat{c}_x, \hat{c}_r, \hat{\theta})$ are the molecular velocity vectors of interacting particles and the kernel is calculated as

$$\tilde{K}(c_x, c_r, \hat{c}_x, \hat{c}_r) = 2 \int\limits_{0}^{\pi} K(c_x, c_r, \hat{c}_x, \hat{c}_r, \beta) \cos\beta \mathrm{d}\beta, \ \beta = \theta - \hat{\theta}. \quad (6)$$

The functions Ψ_i have been introduced to overcome the kernel singularity when $\mathbf{c} = \hat{\mathbf{c}}$ and may be each of the functions $\Psi_i = \{1, \mathbf{c}, c^2\}$, because of mass, momentum and energy conservation (Sharipov and Bertoldo 2009a). Various functions have been tested and the most computational efficient ones are $\Psi_{VS} = \Psi_{TS} = c_r$. The collision kernel $K(\mathbf{c}, \hat{\mathbf{c}}) = K(c_x, c_r, \hat{c}_x, \hat{c}_r, \beta)$ for the HS potential is given by the simple expression (Vasileiadis et al. 2021)

$$K(\mathbf{c}, \hat{\mathbf{c}}) = \pi g \left[\frac{2}{g^2} \exp\left(\frac{\mathbf{c} \times \hat{\mathbf{c}}}{g}\right)^2 - 1 \right], \quad (7)$$

whilst for an arbitrary intermolecular potential, it is given by the double integral (Ferziger and Kaper 1972; Sharipov and Bertoldo 2009b)

$$K(\mathbf{c}, \hat{\mathbf{c}}) = g \left\{ \int\limits_{0}^{2\pi}\int\limits_{0}^{\pi} \exp\left[-\left(g\cot\frac{\chi}{2}\right)^2 + 2|\mathbf{c} \times \hat{\mathbf{c}}| \cot\left(\frac{\chi}{2}\right)\cos\varepsilon \right] \right.$$
$$\left. \left[\sigma\left(\frac{g}{\sin\frac{\chi}{2}}, \chi\right) + \sigma\left(\frac{g}{\sin\frac{\chi}{2}}, \pi - \chi\right) \right] \frac{\sin\chi}{\sin^4\frac{\chi}{2}} \mathrm{d}\chi\mathrm{d}\varepsilon - \sigma_{\text{tot}} \right\}. \quad (8)$$

In Eqs. (7) and (8), the relative velocity $g = |\mathbf{c} - \hat{\mathbf{c}}|$ and the external cross product $\mathbf{c} \times \hat{\mathbf{c}}$ are:

$$g = \left[(c_x - \hat{c}_x)^2 + c_r^2 + \hat{c}_r^2 - 2c_r\hat{c}_r\cos\beta \right]^{1/2}, \quad (9)$$

$$|\mathbf{c} \times \hat{\mathbf{c}}| = \left[(c_r\hat{c}_r\sin\beta)^2 + (c_x\hat{c}_r)^2 + (\hat{c}_x c_r)^2 - 2c_x\hat{c}_x c_r\hat{c}_r\cos\beta \right]^{1/2}. \quad (10)$$

Also, in Eq. (8), χ, ε are the deflection and azimuthal angles respectively, $\sigma(g, \chi)$ is the dimensionless differential cross section (DCS) and σ_{tot} is the dimensionless total cross section (TCS) computed as

$$\sigma_{\text{tot}}(g) = 2\pi \int\limits_{0}^{\pi} \sigma(g, \chi)\sin\chi\mathrm{d}\chi. \quad (11)$$

TCS in the quantum theory of binary collisions is well defined, whilst in the classical one, it is determined using the deflection angle cutoff. In the present work, the DCS is computed via the AI potentials, reported in Cybulski and Toczyłowski (1999), Przybytek et al. (2010), Cencek et al. (2012), Hellmann et al. (2008), Patkowski and Szalewicz (2010), Jäger et al. (2009), Jäger et al. (2016), Jäger and Bich (2017), Haley and Cybulski (2003) and Hellmann et al. (2017), with quantum and classical scattering as described in Sharipov (2022). The employed dense databases of the DCS in terms of the relative speed g and deflection angle χ for the working gases are available in the supplementary material. The associated description, along with a brief discussion on the methodology to obtain the AI potentials, is provided in Appendix 1.

Turning next to the boundary conditions, at the wall $x = 0$, both the MBC and the CLB have been applied following the

description in Basdanis et al. (2022). The linearized outgoing distributions of both problems with MBC read as

$$Y_i(0, c_x, c_r) = (1 - \alpha_M) Y_i(0, -c_x, c_r), \ c_x > 0, \ i = VS, TS, \tag{12}$$

where (c_x, c_r) and (c'_x, c'_r) are the components of the molecular velocity vectors of the reflected and incident particles respectively. Also, $0 < a_M \leq 1$ is the accommodation coefficient, with $\alpha_M = 1$ referring to the DBC. The corresponding outgoing distributions for the CLB read as

$$Y_i(0, c_x, c_r) = \int_{c'_r} \int_{c'_x < 0} A(c'_x, c_x) B(c'_r, c_r)$$
$$Y_i(0, c'_x, c'_r) dc'_x \, dc'_r, \ c_x > 0, \ , \ i = VS, TS. \tag{13}$$

The kernels $A(c'_x, c_x)$, $B(c'_r, c_r)$ and $C(c'_r, c_r)$ are as follows:

$$A(c'_x, c_x) = \frac{2|c'_x|}{\alpha_n} \exp\left(-\frac{c'^2_x + (1 - \alpha_n)c^2_x}{\alpha_n}\right) \times I_0\left(\frac{2\sqrt{1 - \alpha_n}c_x c'_x}{\alpha_n}\right), \tag{14}$$

$$B(c'_r, c_r) = \frac{2c'_r}{\alpha_t(2 - \alpha_t)} \exp\left(-\frac{c'^2_x + (1 - \alpha_t)^2 c^2_r}{\alpha_t(2 - \alpha_t)}\right)$$
$$\times I_1\left(\frac{2(1 - \alpha_t)c_r c'_r}{\alpha_t(2 - \alpha_t)}\right). \tag{15}$$

The parameters $\alpha_t \in [0, 2]$ and $\alpha_n \in [0, 1]$ are the tangential momentum and normal kinetic energy accommodation coefficients respectively. For the specific cases of $\alpha_n = 0$ and $\alpha_t = 2$, the CLB is treated as described in Basdanis et al. (2022).

Far from the wall, as $x \to \infty$, the perturbed distributions are independent of x, i.e.

$$\frac{\partial Y_i(x, c_x, c_r)}{\partial x} = 0, \ i = VS, TS. \tag{16}$$

The LBE (3) along with the complementary expressions (4–8) and the boundary conditions (12–16) may be solved for various values of the accommodation coefficients to obtain the unknown distribution functions $Y_i(x, c_x, c_r)$, $i = VS, TS$. Then, the associated perturbed dimensionless macroscopic distributions may be computed by the moments of the distribution functions. The macroscopic velocity and the heat flux distributions in the $y-$ direction, parallel to the plate are given by

$$u_{y,i}(x) = \frac{1}{\sqrt{\pi}} \int_{-\infty}^{\infty} \int_0^{\infty} Y_i(x, c_x, c_r) \exp\left(-c^2_x - c^2_r\right) c^2_r dc_r dc_x,$$
$$i = VS, TS, \tag{17}$$

$$q_{y,i}(x) = \frac{1}{\sqrt{\pi}} \int_{-\infty}^{\infty} \int_0^{\infty} Y_i(x, c_x, c_r)\left(c^2_x + c^2_r - \frac{5}{2}\right)$$
$$\exp\left(-c^2_x - c^2_r\right) c^2_r dc_r dc_x, \ i = VS, TS, \tag{18}$$

whilst the number density, temperature and pressure are identically equal to zero.

Finally, VSC and TSC are calculated by the asymptotic solution of the corresponding perturbed macroscopic distribution far from the wall as:

$$VSC : \sigma_P = \lim_{x \to \infty} u_{y,VS}(x), \tag{19}$$

$$TSC : \sigma_T = 2 \lim_{x \to \infty} u_{y,TS}(x). \tag{20}$$

Furthermore, VSC and TSC problems are coupled via the reciprocity relation (Sharipov 2016, 2006)

$$\sigma_T = \frac{2}{\sqrt{\pi}} \int_{-\infty}^{\infty} \int_0^{\infty} c_x c_r h^{(\mu)}(c_x, c_r) h^{(\kappa)}(c_x, c_r)$$
$$e^{-(c^2_x + c^2_r)} dc_r dc_x - 2Q_{VS}, \tag{21}$$

where the heat flux of the VSC problem is computed as

$$Q_{VS} = \int_0^{\infty} q_{VS}(x) dx, \tag{22}$$

and $h^{(\mu)}(c_x, c_r)$, $h^{(\kappa)}(c_x, c_r)$ are the perturbation functions resulting from the problems of viscosity and thermal conductivity described in Sharipov (2016) and Sharipov and Bertoldo (2009a). The reciprocity relation (21) is applied for benchmarking purposes to validate the numerical scheme and in several cases to compute the TSC in order to reduce the computational effort.

It is noted that the computation of $h^{(\mu)}(c_x, c_r)$, $h^{(\kappa)}(c_x, c_r)$ in the reciprocity relation and of the viscosity μ and thermal conductivity κ coefficients must be performed in a compatible coordinate system with those of σ_P, σ_T. Therefore, the formulation must be accordingly modified by taking the linear dependence of the gas temperature parallel, rather than normal to the wall. Also, it is clarified that the computation of the viscosity μ is needed in the solution of the LBE, given by Eq. (3). The revised formulation of computing $h^{(\mu)}(c_x, c_r)$, $h^{(\kappa)}(c_x, c_r)$ and the associated transport coefficients are shown in Appendix 2, whilst the employed dimensionless values of μ (and of κ although are not used) with HS and AI potentials are provided in tabulated form in Sect. 4.1.

As pointed out in the introduction, the slip coefficients may also be computed, in an indirect manner, via the corresponding slab problems in the slip regime for large values

of the gas rarefaction parameter $\delta = H/l_0$, with H denoting the distance between the plates. VSC can be estimated by solving the planar Couette or Poiseuille flows to compute the dimensionless shear stress Π or flow rate G_P respectively and then deduce σ_P from expression (104) in Sharipov (2011). Similarly, TSC can be estimated by solving the planar thermal creep flow to compute the dimensionless flow rate G_T and then deduce σ_T from expression (137) in Sharipov (2011). The formulation of the Couette, Poiseuille and thermal creep problems with the LBE and DBC is provided, for completeness purposes, in Appendix 3. Comparisons of the VSC and TSC deduced by the two approaches are performed and, in all cases, an agreement within the numerical error is observed.

3 Numerical scheme

The LBE with HS and AI potential, subject to MBC and CLB is numerically solved by applying a 2nd-order central finite-difference scheme in the physical space and the discrete velocity method in the molecular velocity space. Then, the discretised equations are solved in an iterative manner. The numerical scheme is similar to that applied in Basdanis et al. (2022); Vasileiadis et al. 2021).

The physical space $x \in [0, 10]$ is divided into N equal segments $\Delta x = 10/N$, with $N + 1$ nodes x_l, $l = 1, 2, \ldots, N + 1$. The computational domain of the ten equivalent mean free paths is adequate in order to provide grid independent results at the reported significant digits for the slip coefficients, in the physical space. This is confirmed using 15 equivalent free paths and deducing identical corresponding values for the slip coefficient. Next, the continuum molecular velocity space $\mathbf{c} = (c_x, c_r, \theta)$ is discretised as follows.

- The spectrum of x-component of the molecular velocity $c_x \in (-\infty, \infty)$ is divided into two parts: $c_x \in (-\infty, 0]$, $c_x \in [0, \infty)$. Each part is replaced by a set of discrete molecular velocities as $-c_{x,k}$ and $c_{x,k}$, with $k = 1, 2, \ldots, Nc_x/2$ and the values $c_{x,k}$ are taken to be the roots of the half-range Hermite polynomials of degree $Nc_x/2$, with weights w_k. The total number of discrete velocities in the $x-$ direction is Nc_x.
- Similarly, the spectrum of the r-component of the molecular velocity $c_r \in [0, \infty)$ is replaced by a set of discrete molecular velocities $c_{r,m}$, with $m = 1, 2, \ldots, Nc_r$. The values $c_{r,m}$ are taken to be the roots of the half-range Hermite polynomials of degree Nc_r with weights w_m.
- The spectrum of the angle $\beta \in [0, \pi]$ ($\beta = \theta - \hat{\theta}$) is replaced by a set of angels β_t, with $t = 1, 2, \ldots, N_\beta$ and the values β_t are taken to be the roots of the Legendre polynomials of degree N_β accordingly transformed from $[-1, 1]$ to $[0, \pi]$ with weights w_t.

Furthermore, once the discrete set $\{c_{x,k}, c_{r,m}, \beta_t\}$ is chosen, the collision kernel $\tilde{K}(c_x, c_r, \hat{c}_x, \hat{c}_r)$ in Eq. (6) is numerically integrated over β and stored. Its computation is based on the estimation of the associated kernels $K(c_x, c_r, \hat{c}_x, \hat{c}_r, \beta)$, given in Eqs. (7) and (8) for the HS and AI potentials respectively. The computation for the HS potential is straightforward since K is explicitly defined in Eq. (7). On the contrary, for the AI potential with either quantum or classical scattering, each component of K is computed via a double numerical integration over the deflection angle χ and the azimuthal angle ϵ, as defined in Eq. (8). In this framework, a dense database of the DCS $\sigma(g, \chi)$ for each investigated gas is employed, in terms of the relative velocity g and the deflection angle χ. The deflection angle χ is divided into N_χ segments in the interval $[0, \pi]$ and similarly the azimuthal angle ϵ is divided into N_ϵ segments in the interval $[0, 2\pi]$. The integrations with respect to χ and ϵ are performed via the trapezoidal rule. Obviously, the computational effort of estimating kernel K, is significantly increased in the case of the AI potential, compared to the HS. It is noted however, that this computation is performed only once for each set $\{c_x, c_r, \hat{c}_x, \hat{c}_r\}$ and then it is stored and used in each iteration of the scheme.

Based on the above, the unknown discretised distribution functions are defined as

$$Y_{i,l,k,m} = Y_i(x_l, c_{x,k}, c_{r,m}), \ i = \text{VS}, \text{TS}, \ l = 1, 2, \ldots,$$
$$N + 1, \ k = 1, 2, \ldots, Nc_x, \ m = 1, 2, \ldots, Nc_r, \qquad (23)$$

whilst the discretised version of Eqs. (3), (5) and (6) is as follows:

$$c_{x,k} \frac{Y_{i,l+1,k,m}^{(n)} - Y_{i,l,k,m}^{(n)}}{\Delta x} + a\mu v_{0,k,m}^b \left(Y_{i,l+1,k,m}^{(n)} + Y_{i,l,k,m}^{(n)} \right)$$
$$= \mu \sum_{c=1}^{Nc_x} \sum_{d=1}^{Nc_r} \Lambda_{k,m,c,d} \left[Y_{i,l+1,c,d}^{(n-1)} + Y_{i,l,c,d}^{(n-1)} \right.$$
$$\left. - \frac{\Psi_{i,c,d}}{\Psi_{i,k,m}} \left(Y_{i,l+1,k,m}^{(n-1)} + Y_{i,l,k,m}^{(n-1)} \right) \right] + s_i(c_{x,k}, c_{r,m})$$
$$+ a\mu v_{0,k,m}^b \left(Y_{i,l+1,k,m}^{(n-1)} + Y_{i,l,k,m}^{(n-1)} \right), \qquad (24)$$

$$\Lambda_{k,m,c,d} = \frac{1}{\pi^{3/2}} K_{k,m,c,d} c_{r,d} e^{-\left(c_{x,c}^2 + c_{r,d}^2 \right)} w_c w_d, \qquad (25)$$

$$K_{k,m,c,d} = 2 \sum_{t=1}^{N_\beta} K_{k,m,c,d,t} w_t. \qquad (26)$$

The unknown distributions are computed in an iterative scheme, with the superscript (n) denoting the iteration index. The last term in the left- and right-hand sides of Eq. (24) have been included as conditioners to speed up the convergence of the iterative scheme (Sharipov and Bertoldo 2009b), with $v_{0,k,m}^b$

being the collision frequency for HS potential, whilst a and b are empirical tuning parameters.

The discretised macroscopic quantities are obtained via half-range Hermite quadrature as

$$u_{y,i,l}^{(n)} = \frac{1}{\sqrt{\pi}} \sum_{k=1}^{Nc_x} \sum_{m=1}^{Nc_r} Y_{i,l,k,m}^{(n)} \exp\left(-c_{x,k}^2 - c_{r,m}^2\right) c_{r,m}^2 w_k w_m, \quad i = \text{VS, TS,}$$

$$(27)$$

$$q_{y,i,l}^{(n)} = \frac{1}{\sqrt{\pi}} \sum_{k=1}^{Nc_x} \sum_{m=1}^{Nc_r} Y_{i,l,k,m}^{(n)} \left(c_{x,k}^2 + c_{r,m}^2 - \frac{5}{2}\right)$$
$$\exp\left(-c_{x,k}^2 - c_{r,m}^2\right) c_{r,m}^2 w_k w_m, \quad i = \text{VS, TS.}$$

$$(28)$$

The iterative scheme is initiated by setting $Y_{i,l,k,m}^{(1)} = 0$ at the right-hand side of Eq. (24), and the iterations are repeated upon convergence. In each iteration, a marching scheme is applied in the physical space to compute $Y_{i,l,k,m}^{(n)}$ for each molecular velocity (no matrix inversion is needed). Starting from the wall and for all positive velocities $c_{x,k} > 0$, $Y_{i,1,k,m}^{(n)}$ is computed at $x = 0$, based on the implemented boundary conditions Eqs. (12–15). Then, marching away from the wall, $Y_{i,l,k,m}^{(n)}$ is computed at all physical nodes $l = 2, \ldots, N+1$ and for positive velocities $c_{x,k} > 0$. Next, far from the wall, at $x = 10$ and for all negative velocities $c_{x,k} < 0$, $Y_{i,N+1,k,m}^{(n)}$ is computed by substituting boundary condition (16) into Eq. (24) to yield

$$Y_{i,N+1,k,m}^{(n)}$$
$$= Y_{i,N+1,k,m}^{(n-1)} + \frac{1}{a\mu v_{0,k,m}^b} \left\{ \mu \sum_{c=1}^{Nc_x} \sum_{d=1}^{Nc_r} \Lambda_{k,m,c,d} \left[Y_{i,N+1,c,d}^{(n-1)} \right. \right.$$
$$\left. \left. - \frac{\Psi_{i,c,d}}{\Psi_{i,k,m}}\left(Y_{i,N+1,k,m}^{(n-1)}\right)\right] + s_i\left(c_{x,k}, c_{r,m}\right) \right\}.$$

$$(29)$$

Finally, marching from $x = 10$ towards the wall, $Y_{i,l,k,m}^{(n)}$ is computed at all physical nodes $l = N, N-1, \ldots, 1$ and for negative velocities $c_{x,k} < 0$. At the end of each iteration, all the macroscopic quantities according to Eqs. (27–28) are computed.

The iterative scheme is concluded when the following convergence criteria is fulfilled:

$$\frac{1}{2(N+1)} \sqrt{\sum_{l=1}^{N+1} \left(u_{i,l}^{(n)} - u_{i,l}^{(n-1)}\right)^2 + \sum_{l=1}^{N+1} \left(q_{i,l}^{(n)} - q_{i,l}^{(n-1)}\right)^2}$$
$$< 10^{-9}, \quad i = \text{VS, TS.}$$

$$(30)$$

Suitable values of the convergence speed-up parameters a and b have been chosen. For HS, $a = b = 1$, whilst for AI, $a = 0.8$, $b = 3$ for quantum scattering and $a = 8$, $b = 3$ for classical scattering. Furthermore, the employed parameters ensure a numerical error of less than 0.5% in the reported data of the slip coefficients. The results provided here for

Table 1 Computational time and number of iterations for VSC and TSC based on HS, LJ and AI potentials in various numerical grids (LBE with DBC; employed gas: He)

Potential	Grid $(\text{Nc}_x, \text{Nc}_r)$	Cores	Iterations	Computational time (h)
HS	64×32	64	4000	0.7
LJ	64×32	256	85,000	3.7
AI quantum	64×32	256	85,000	3.5
AI classical	64×32	256	150,000	5.4

the VSC and TSC are with $N = 300$, $Nc_x = 64$, $Nc_r = 32$, $N_\beta = 100$, $N_\varepsilon = 100$ and $N_\chi = [800 - 2000]$ depending on the gas.

Some insight in the involved computational effort is given in Table 1, where indicative data of the computational time and the number of iterations, needed for convergence of the iterative scheme, are provided for the VSC and TSC with HS, LJ and AI potentials. The computations with the LJ potential have been performed in order to have the comparison on the same basis. In both problems, the number of iterations and the computational time of the AI with quantum scattering and the LJ potentials are about 20 times larger than of the HS potential, whilst the corresponding quantities of the AI potential with classical scattering are about two times larger than the AI quantum one (40 times larger compared to HS). Comparing the AI with the LJ potentials, it is seen that the AI with quantum scattering is slightly faster. It is concluded that the implementation of the AI and LJ potentials in the LBE, compared to the HS one, even by precalculating and storing the collision kernel $\tilde{K}\left(c_x, c_r, \hat{c}_x, \hat{c}_r\right)$, significantly increases the required computational time and this is due to the increased number of iterations upon convergence (Table 1). On the contrary, in the DSMC method, the corresponding increase of the computational time is the modest (Sharipov and Strapasson 2012a, b).

4 Results and discussion

Numerical results are provided for the viscous (VSC) and thermal (TSC) slip coefficients via the LBE with HS and AI potentials, subject to diffuse (DBC), Maxwell (MBC) and Cercignani–Lampis (CLB) boundary conditions. Based on the data with the HS potential, interpolating expressions are deduced in terms of the accommodation coefficients for the MBC and CLB, using symbolic regression based on genetic programming (Cranmer et al. 2020). The data with the AI potential, include quantum and classical scattering and of course depend on the gas and gas temperature. The employed gases are He, Ne, Ar, Kr and Xe at temperature 300 K, whilst in the case of He, the VSC and the TSC are

provided with quantum and classical scattering in a wide range of temperature in order to investigate the importance of the quantum effects. Comparisons with corresponding data obtained via the linearized Shakhov kinetic model are performed.

It is noted that the reliability of the employed AI potentials has been verified by comparing the numerical values of viscosity based on the AI potential reported in Cencek et al. (2012), Sharipov and Benites (2021), Sharipov and Benites (2020) with those measured experimentally in Berg and Burton (2013). It is deduced that the largest disagreement of 0.12% is observed for neon, whilst it is quite smaller for the other gases.

The employed transport coefficients are provided in Sect. 4.1, the VSC and the TSC data are given and discussed in Sects. 4.2 and 4.3 respectively and the quantum and classical approaches are compared in Sect. 4.4.

4.1 Viscosity and thermal conductivity with AI potential

Based on the formulation presented in Appendix 2 and the discretization parameters specified in Sect. 3, the dimensionless viscosity and the thermal conductivity with HS and AI potential, with quantum scattering at 300 K, as well as the corresponding dimensional ones, are given in Table 2. The dimensional bulk quantities are obtained as:

$$\mu' = \left(m v_0 \mu\right)/d^2, \tag{31}$$

$$\kappa' = \left(k_B v_0 \kappa\right)/d^2. \tag{32}$$

Here, d denotes the zero point of the AI potential and is given in Table 13. Then, their relative difference with the corresponding ones, based also on the AI potential (Cencek et al. 2012; Jäger et al. 2016; Hellmann et al. 2017; Sharipov and Benites 2021; Bich et al. 2008; Vogel et al. 2010), as well as on the LJ potential (Sharipov and Bertoldo 2009a) is less than 1%. Also, the present HS results (last column) agree to at least 4 significant figures with the HS ones in Siewert (2002); Mohan et al. (2008).

Furthermore, in Table 3, the dimensionless viscosity and the thermal conductivity of He with AI potential for quantum and classical scattering at various temperatures from

Table 3 Dimensionless viscosity and thermal conductivity of He based on AI potential at various temperatures; comparison between classical and quantum scattering

Temperature (K)	Viscosity (μ)		Thermal conductivity (κ)	
	Classical	Quantum	Classical	Quantum
1	0.03227	0.05350	0.1214	0.2065
10	0.07577	0.1082	0.2852	0.4080
10^2	0.1536	0.1552	0.5802	0.5880
3×10^2	0.1869	0.1868	0.7042	0.7066
10^3	0.2385	0.2385	0.8993	0.9012
10^4	0.4509	0.4510	1.704	1.705

1 K up to 10^4 K are provided. At any temperature, the gas pressure should be lower than the corresponding saturated vapour pressure in order to meet the conditions of dilute gas.

The results via quantum scattering have a relative difference of less than 0.6% with the corresponding ones in Cencek et al. (2012). For temperatures equal and larger than 300 K, the values of μ, with the quantum and classical approaches (as well as of κ), agree up to at least three significant. On the contrary, at 100 K differences between the corresponding values of quantum and classical scattering start to appear, which are increased as the temperature is decreased. At temperatures 10 K and 1 K, the relative differences between the quantum and classical approaches reach about 30% and 40% respectively, both in μ and κ, implying that in the estimation of the transport coefficients at low temperature, quantum effects must be considered.

In the present work, the viscosity data provided in Tables 2 and 3 are used in the solution of the LBE to deduce the VSC and the TSC, whilst the thermal conductivity data are provided mainly for completeness purposes and future reference. The comparison between quantum and classical scattering is limited only to He, where the effect of quantum phenomena is the strongest one amongst all gases considered here.

4.2 Viscous slip coefficient

The half-space velocity viscous slip problem, also known as the Kramers problem, defined in Sect. 2, has been

Table 2 Viscosity and thermal conductivity via the LBE based on AI and quantum scattering at $T_0 = 300$ K

Gas	He	Ne	Ar	Kr	Xe	HS
Dimensionless viscosity (μ)	0.1868	0.1457	0.1091	0.09600	0.08313	0.12667
Viscosity (μ') [μPa s]	19.87	31.84	22.68	25.42	23.20	
Dimensionless thermal conductivity (κ)	0.7066	0.5529	0.4134	0.3637	0.3150	0.47931
Thermal conductivity (κ') [mW/(m K)]	156.2	49.79	17.89	9.554	5.568	

Table 4 Viscous slip coefficient based on HS, LJ and AI potentials at $T_0 = 300$ K and diffuse boundary conditions

Potential	σ_P				
	He	Ne	Ar	Kr	Xe
HS	0.987	0.987	0.987	0.987	0.987
LJ (Sharipov 2011)	1.00	1.00	1.02	1.02	1.03
AI quantum	0.999	1.00	1.01	1.02	1.02

numerically solved via the LBE with HS and AI potentials, subject to DBC, MBC and CLB. Then, the VSC is computed by Eq. (19).

In Table 4, the VSC is provided for the five monoatomic gases with HS, LJ (Sharipov 2011) and AI potentials at 300 K and DBC ($\alpha_M = 1$). A relative difference of less than 1% is observed between the VSC data with LJ and AI potentials. The VSC slightly increases with the molecular mass. As can be seen, all data, including the HS ones, agree within $\pm 2\%$ with the recommended value of $\sigma_P = 1$ for DBC, independently of the gas.

In Table 5, the VSC data are extended in the case of MBC with $\alpha_M \in [0.2, 1]$. The relative difference in the VSC data between HS and AI potentials is less than 4%. The data based on the HS potential can be approximated by the interpolation expression

$$\sigma_P = \frac{1.773}{\alpha_M} - 0.114\alpha_M - 0.673, \tag{33}$$

which may be applied in the range $0.2 < \alpha_M < 1$ with an error of less than 0.2%. Expression (33) is similar to

Table 5 Viscous slip coefficient based on HS and AI potentials at $T_0 = 300$ K and Maxwell boundary conditions

α_M	σ_P					
	HS	AI quantum				
		He	Ne	Ar	Kr	Xe
0.2	8.17	8.19	8.20	8.22	8.24	8.27
0.4	3.72	3.74	3.74	3.76	3.78	3.79
0.6	2.21	2.23	2.24	2.25	2.26	2.27
0.8	1.45	1.47	1.47	1.48	1.49	1.50
1	0.987	0.999	1.00	1.01	1.02	1.02

Table 6 Viscous slip coefficient based on HS and AI (gas: He) potentials at $T_0 = 300$ K and Cercignani–Lampis boundary conditions

Potentials	α_t	σ_P					
		$\alpha_n = 0$	0.2	0.4	0.6	0.8	1
HS	0.2	8.17	8.15	8.13	8.11	8.09	8.08
	0.4	3.71	3.70	3.68	3.67	3.66	3.65
	0.6	2.21	2.20	2.19	2.18	2.18	2.17
	0.8	1.45	1.45	1.44	1.44	1.43	1.43
	1	0.987	0.987	0.987	0.987	0.987	0.987
	1.2	0.671	0.676	0.681	0.685	0.688	0.692
	1.4	0.440	0.450	0.458	0.466	0.474	0.481
	1.6	0.262	0.276	0.288	0.300	0.311	0.322
	1.8	0.119	0.137	0.153	0.169	0.184	0.198
	2	0	0.0221	0.0425	0.0617	0.0801	0.0978
AI quantum (He)	0.2	8.19	8.16	8.13	8.11	8.09	8.08
	0.4	3.73	3.71	3.70	3.68	3.67	3.65
	0.6	2.23	2.22	2.21	2.20	2.19	2.18
	0.8	1.47	1.46	1.46	1.45	1.45	1.44
	1	0.999	0.999	0.999	0.999	0.999	0.999
	1.2	0.680	0.686	0.691	0.696	0.700	0.704
	1.4	0.446	0.457	0.467	0.476	0.485	0.494
	1.6	0.265	0.281	0.295	0.309	0.323	0.336
	1.8	0.120	0.140	0.159	0.178	0.195	0.212
	2	0	0.0243	0.0476	0.0700	0.0919	0.113

Eq. (105) of Sharipov (2011), based on the HS potential. The present VSC data for the HS potential and MBC, agree in all shown significant digits with those reported in Sharipov (2011).

Next, in Table 6, the VSC data based on HS and AI potentials, subject to CLB are tabulated. The database in terms of $\alpha_t \in [0.2, 2]$ and $\alpha_n \in [0, 1]$ is dense to facilitate future work in the characterisation of the gas–surface interaction via comparisons with experiments. In Table 6, the VSC data with AI potential are only for He, whilst the data of the other gases are available in the supplementary material. For $\alpha_t = 1$, σ_P is independent of α_n, whilst for $\alpha_t < 1$ and $\alpha_t > 1$, as α_n increases, σ_P slightly decreases and increases respectively. The dependency of the VSC on α_n is very weak, except in the case of strong back-scattering ($\alpha_t > 1.5$). Also, the VSC data in Table 6 for $\alpha_t \leq 1$ and $\alpha_n = 0$ are in excellent agreement with the corresponding ones in Table 5 for $\alpha_M \leq 1$. Furthermore, the corresponding VSC data with HS and AI potentials, agree within 4% for $\alpha_t \leq 1.6$, whilst in the cases of strong back-scattering, $\alpha_t = [1.8, 2]$, the disagreement reaches about 13%. Thus, the effect of the intermolecular potential on σ_P may be considered as negligible, unless strong back-scattering is present. The VSC based on HS potential with CLB can be approximated by the interpolation expression

$$\sigma_P = \frac{1.773}{\alpha_t} - 0.786 - 0.00668(1 - 0.978\alpha_n)(10 - \alpha_t)$$
$$(-0.357\alpha_n + \alpha_t + 0.695) \log(\alpha_t),$$
(34)

which can be applied for $0.2 < \alpha_t < 1.6$ and $0 < \alpha_n < 1$ with an error of less than 0.2% and unlike the available expressions in the literature, it captures, not only the strong effect of α_t, but also the weak effect of α_n.

In Fig. 1, the present VSC data based on the LBE, denoted by $\sigma_P^{(HS)}$ and $\sigma_P^{(AI)}$ for the HS and AI potentials, are compared with those $\sigma_P^{(S)}$ obtained via the linearized Shakhov model for the CLB. The values of $\sigma_P^{(S)}$ have been reproduced here, for the values of α_t, α_n in Table 6. It is seen that the relative errors $\left(\sigma_P^{(HS)} - \sigma_P^{(S)}\right)/\sigma_P^{(HS)}$ in Fig. 1a and $\left(\sigma_P^{(AI)} - \sigma_P^{(S)}\right)/\sigma_P^{(AI)}$ in Fig. 1b, remain small for $\alpha_t \leq 1.6$, whilst they significantly increase for $\alpha_t > 1.6$ (particularly in the light species). Thus, the VSC is independent of the implemented kinetic equation, unless strong back-scattering is present in the flow setup.

A more detailed view of the whole Knudsen layer, is shown in Fig. 2, where the dimensionless velocity and the heat flux distributions in the VSC problem via the LBE with HS and AI potentials and the linearized Shakhov kinetic model are plotted. The results based on the AI potential correspond to He and Xe with DBC. The thickness of the Knudsen layer is about 4 equivalent free paths. Although the associated velocity slips at the wall of each approach are different, the velocity distributions inside the Knudsen layer and their asymptotic behaviour far from the wall, which determines the VSC, present relative differences of less than 4%. The heat flux distributions show a similar behaviour. Also, they all tend to zero far from the wall.

In several cases, mainly for benchmarking purposes, the VSC has been also deduced, following the indirect formulation of Appendix 3. For example, in the case of HS potential and DBC the value of the VSC, extracted by solving the half-space problem is $\sigma_P = 0.987$ (Table 4). Exactly the same result is deduced by solving the Couette flow for $\delta \geq 10$ or the Poiseuille flow for $\delta \geq 80$.
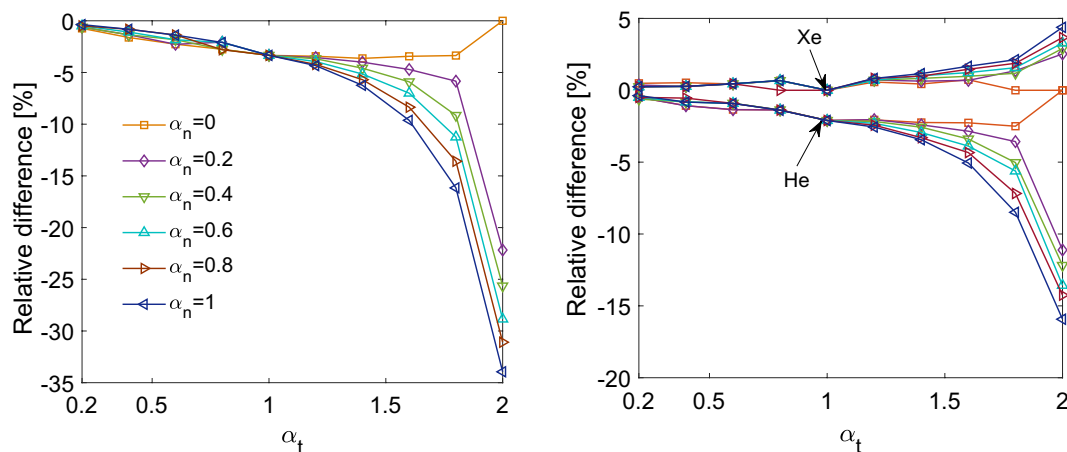

Fig. 1 Relative difference of the VSC data of the linearized Shakhov model with respect to the LBE based on HS potential (left) and AI potential for He and Xe (right)
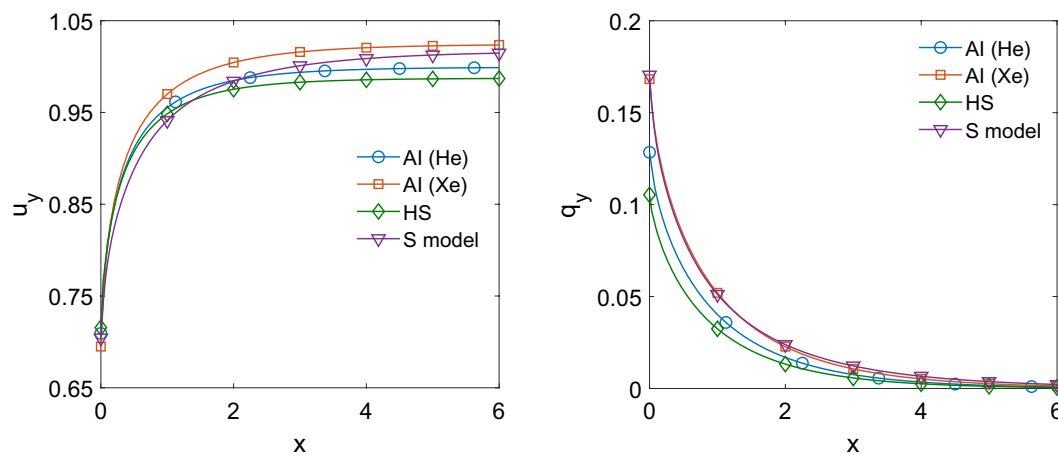
Fig. 2 Dimensionless velocity (left) and heat flux (right) profiles in the VSC problem with DBC via the LBE based on HS and AI (gases: He, Xe) potentials and the linearized Shakhov kinetic model

Table 7 Thermal slip coefficient based on HS, LJ and AI potentials at $T_0 = 300$ K and diffuse boundary conditions

Potential	σ_T				
	He	Ne	Ar	Kr	Xe
HS	1.02	1.02	1.02	1.02	1.02
LJ (Sharipov 2011)	1.08	1.07	1.13	1.16	1.18
AI quantum	1.07	1.07	1.12	1.15	1.17

4.3 Thermal slip coefficient

The half-space velocity thermal slip problem, defined in Sect. 2, is numerically solved via the LBE with HS and AI potentials, subject to DBC, MBC and CLB, and then, the TSC is computed by Eq. (20). Alternatively, the TSC may be deduced from the reciprocity relation (21). The double integral at the right-hand side of Eq. (21) is calculated only once (independent of the boundary conditions) and then, σ_T is readily deduced through the heat flux Q_{VS} of the VSC problem. Here, the reciprocity relation (21) has been used mainly for benchmarking purposes and it always accurately fulfilled.

In Table 7, the TSC is provided for the five monoatomic gases with HS, LJ and AI potentials at 300 K and diffuse boundary conditions ($\alpha_M = 1$). The TSC for the HS potential is $\sigma_T = 1.02$ and agrees in all significant figures shown, with the reported one (Sharipov 2011; Sone et al. 1989), whilst the values of the TSC with AI potential for the five monoatomic gases are almost identical to the ones with the LJ potential (Sharipov 2011). The differences between the TSC with HS and AI (or LJ) potentials are more significant than in the VSC and more specifically, they are about 6% for He and they increase with the molecular mass of the gas, reaching up to about 15% for Xe. The recommended value of $\sigma_T = 1.1$ is reasonable, since it is in the middle of the TSC data range for the five monoatomic gases with AI (or LJ) potential.

In Table 8, the TSC data with HS and AI potentials at 300 K are given for MBC, with $\alpha_M \in [0.2, 1]$. The deviations between the TSC based on the HS and AI potentials for all five gases with $\alpha_M < 1$ are quantitatively similar as

Table 8 Thermal slip coefficient based on HS and AI potentials at $T_0 = 300$ K and Maxwell boundary conditions

α_M	σ_T					
	HS	AI quantum				
		He	Ne	Ar	Kr	Xe
0.2	0.831	0.838	0.837	0.839	0.844	0.845
0.4	0.881	0.903	0.902	0.918	0.929	0.934
0.6	0.929	0.965	0.963	0.992	1.01	1.02
0.8	0.975	1.02	1.02	1.06	1.08	1.10
1	1.02	1.08	1.07	1.12	1.15	1.17

for $\alpha_M = 1$. It is useful to note that, unlike the VSC, the TSC decreases as the gas reflection at the wall reflection becomes more specular, which is reasonable considering the driving force mechanism in the thermal creep flow. The TSC with the HS potential and MBC can be approximated by the interpolation expression

$$\sigma_T = 0.7789 + 0.2667\alpha_M - 0.02667\alpha_M^2, \qquad (35)$$

which can be applied in the range $0.2 \leq \alpha_M \leq 1$ with an error of less than 0.1%. Expression (35) is more complex than Eq. (138) in Sharipov (2011) but fits the data better. The reported TSC data with HS potential and MBC are in excellent agreement with the ones cited in Sharipov (2011).

In Table 9, the TSC data with HS and AI potential, subject to CLB are tabulated. In this case, the available data in the literature are mainly limited to the HS potential. There is only one recent work via the LBE with the variable hard sphere model and CLB, where TSC data for monatomic gases are reported by solving the slab thermal creep flow for a limited number of CLB accommodation coefficients (Wang et al. 2020). Here, as in the VSC, the data are based on the solution of the half-space problem for many values of $\alpha_t \in [0.2, 2]$ and $\alpha_n \in [0, 1]$. In Table 9, the TSC data with AI potential are only for He, whilst for the other gases, the data are available in the supplementary material. In order to have a graphical view of the dependency of σ_T on (α_t, α_n), the TSC data for He in Table 9, along with the ones in Table 8
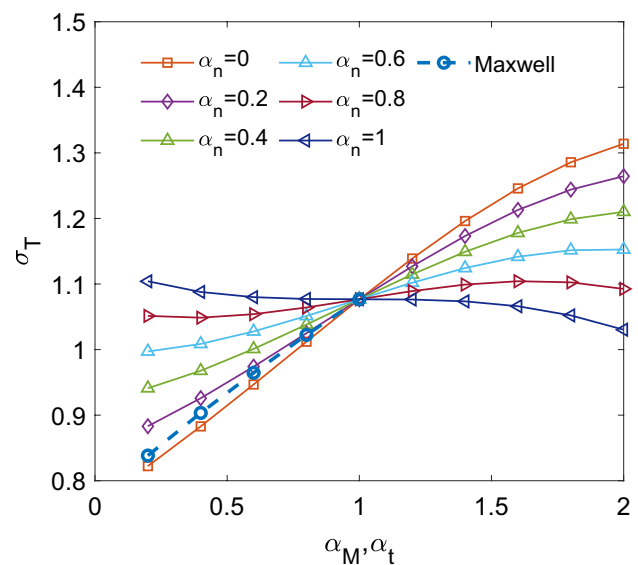
Fig. 3 TSC data for He based on AI potential at $T_0 = 300$ K vs the accommodation coefficients of the CLB and MBC

for the MBC, are plotted in Fig. 3. Clearly, σ_T depends on both α_t and α_n. There is a resemblance between the MBC ($\alpha_M < 1$) and CLB data for $\alpha_t \leq 1$ and $\alpha_n = 0$, and of course the data coincide when $\alpha_M = \alpha_t = 1$, independently of α_n. Furthermore, the dependency of the TSC on α_t is strong at small values of α_n and is rather weak as α_n approaches

Table 9 Thermal slip coefficient based on HS and AI (gas: He) potentials at $T_0 = 300$ K and Cercignani–Lampis boundary conditions

Potentials	a_t	σ_T					
		$a_n = 0\,0$	0.2	0.4	0.6	0.8	1
HS	0.2	0.807	0.861	0.914	0.965	1.01	1.06
	0.4	0.850	0.889	0.927	0.964	1.00	1.04
	0.6	0.902	0.927	0.952	0.976	1.00	1.02
	0.8	0.959	0.971	0.983	0.995	1.01	1.02
	1	1.02	1.02	1.02	1.02	1.02	1.02
	1.2	1.07	1.06	1.05	1.04	1.03	1.02
	1.4	1.13	1.10	1.08	1.06	1.04	1.01
	1.6	1.17	1.14	1.10	1.07	1.04	1.00
	1.8	1.20	1.16	1.11	1.07	1.02	0.979
	2	1.21	1.16	1.11	1.06	1.00	0.944
AI quantum (He)	0.2	0.822	0.883	0.941	0.997	1.05	1.10
	0.4	0.883	0.926	0.968	1.01	1.05	1.09
	0.6	0.947	0.974	1.00	1.03	1.05	1.08
	0.8	1.01	1.03	1.04	1.05	1.06	1.08
	1	1.08	1.08	1.08	1.08	1.08	1.08
	1.2	1.14	1.13	1.11	1.10	1.09	1.08
	1.4	1.20	1.17	1.15	1.12	1.10	1.07
	1.6	1.25	1.21	1.18	1.14	1.10	1.07
	1.8	1.29	1.24	1.20	1.15	1.10	1.05
	2	1.31	1.26	1.21	1.15	1.09	1.03

one. More specifically, as α_t increases, the TSC for $\alpha_n \leq 0.4$ monotonically increases, for $\alpha_n = [0.6, 0.8]$ changes non-monotonically and for $\alpha_n = 1$ monotonically decreases. The dependency of the TSC on α_n is strong for small and large values of α_t and gradually diminishes as $\alpha_t \to 1$. The relative deviations of the TSC between the HS and AI for each gas results remain about the same as in the case of DBC.

The TSC with the HS potential and CLB may be approximated by the interpolation expression

$$\sigma_T = 1.018 + 0.0124(1 - \alpha_t)$$
$$\left[(1 - \alpha_n)(2.19\alpha_t - 25.7) + 6.84(0.958\alpha_t - 1)^2 \right],$$
(36)

which can be used in the ranges $0.4 \leq \alpha_t \leq 1.8$ and $0 \leq \alpha_n \leq 1$ with an error of less than 0.4%.

The relative differences between TSC data for the HS and AI potentials, $\sigma_T^{(HS)}$ and $\sigma_T^{(AI)}$ respectively and the corresponding ones $\sigma_T^{(S)}$ by the linearized Shakhov model, reproduced here for the purposes of the present work, are potted in Fig. 4. The relative errors $\left(\sigma_T^{(HS)} - \sigma_T^{(S)} \right)/\sigma_T^{(HS)}$ in Fig. 4a and $\left(\sigma_T^{(AI)} - \sigma_T^{(S)} \right)/\sigma_T^{(AI)}$ in Fig. 4b are significant, except in the case of Xe, where, coincidentally, the errors are small. Thus, it is confirmed that the TSC depends on the implemented kinetic equation and intermolecular potential.

The dimensionless velocity and the heat flux distributions in the TSC problem via the LBE with HS and AI (gases: He and Xe) potentials and the linearized Shakhov kinetic model are plotted in Fig. 5. The plots are for DBC. The thickness of the Knudsen layer is about 5 equivalent mean free paths. The differences are significant in the velocity slips at the wall, as well as in the velocity distributions, whilst they are almost negligible in the heat flux distributions. In the
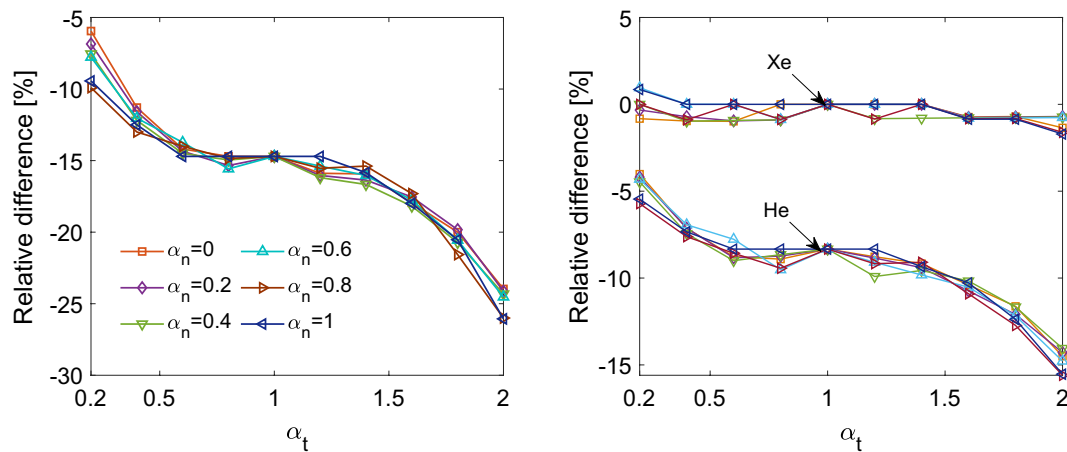
Fig. 4 Relative difference of the TSC data of the linearized Shakhov model with respect to the LBE based on HS potential (left) and AI potential for He and Xe (right)
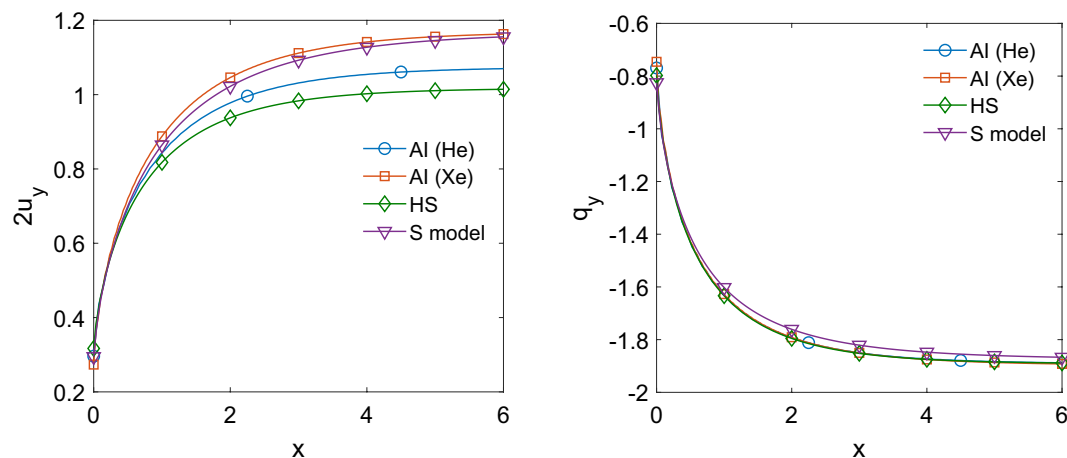

Fig. 5 Dimensionless velocity (left) and heat flux (right) profiles in the TSC problem with DBC via the LBE based on HS and AI (gases: He, Xe) potentials and the linearized Shakhov kinetic model

velocity distributions, the one of the linearized Shakhov model almost coincides with the one of Xe, but it is far away from the one of He.

The TSC may also be deduced, following the indirect formulation of Appendix 3. Indicatively, the value of $\sigma_T = 1.02$ obtained with HS potential and DBC (Table 7), may be reproduced by solving the plane thermal creep (or transpiration) flow for $\delta \geq 80$.

4.4 Quantum vs classical AI at various temperatures

Recently, by employing the AI potential with quantum and classical scattering in the Couette and Fourier flows, differences have been observed in the computed shear stresses and heat fluxes respectively of light gases, at temperatures less than 300 K (Sharipov 2018b). Here, a similar study is performed for the slip coefficients. The importance of the quantum effects in the estimation of the VSC and TSC is investigated, by considering quantum and classical approaches in the case of He with AI potential. Although the deviations from the classical behaviour are expected at low temperatures, the investigation includes a wide range of temperatures from 1 K up to 10^4 K. For temperatures below the boiling

point of He (4.2 K at 1 atm), the pressure must be accordingly decreased to keep He in the gaseous phase.

The computed data of σ_P and σ_T are provided in Table 10 and in Fig. 6, based on DBC. VSC and TSC values of He with the quantum approach at 300 K are the ones in Tables 4 and 7 respectively. The VSC data remain almost constant in the whole range of temperatures and the differences between the classical and quantum approaches is negligible. On the contrary, TSC data depend on temperature. Also, differences between the classical and quantum approaches start to appear at 100 K and they increase as the temperature decreases, reaching about 15% at 1 K. It is concluded that

Table 10 VSC and TSC data of He based on AI potential considering classical and quantum scattering at various temperatures

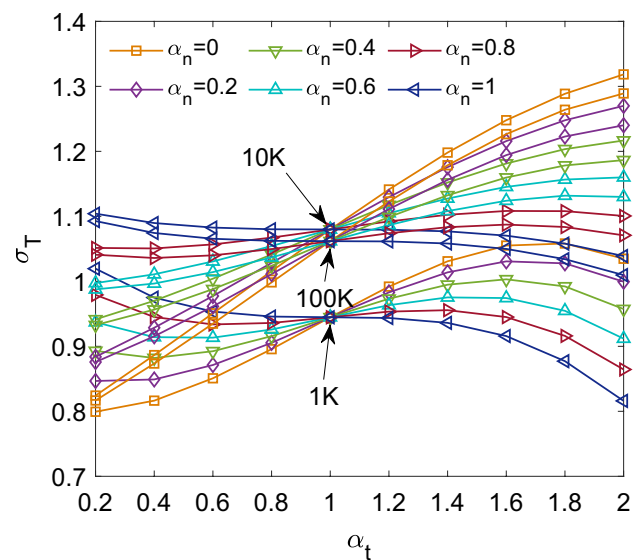| Temperature (K)	σ_P		σ_T	
	Classical	Quantum	Classical	Quantum
1	1.01	0.980	1.12	0.945
10	1.02	1.00	1.18	1.08
10^2	1.00	0.997	1.08	1.06
3×10^2	1.00	0.999	1.07	1.07
10^3	1.00	1.00	1.08	1.09
10^4	1.01	1.01	1.12	1.12

Fig. 7 TSC data for He based on AI potential and quantum scattering at $T_0 = 1$ K, 10 K and 100 K vs the accommodation coefficients of the CLB
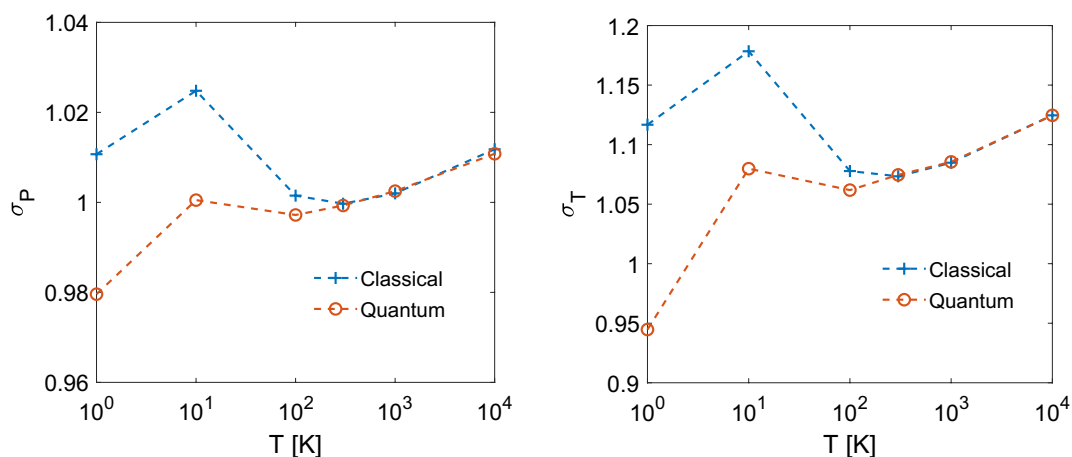

Fig. 6 VSC and TSC data for He based on AI potential considering classical and quantum scattering vs temperature

quantum effects are not important in the computation of σ_P, but they play an important role in the computation of σ_T and should be considered at low temperatures. In Fig. 7, the TSC of He with AI potential at 1, 10 and 100 K for various values of the accommodation coefficients of the CLB is plotted. As the temperature decreases the qualitative behaviour remains the same, but the TSC data change significantly. As observed in Figs. 6 and 7, the dependence of VSC and TSC on temperature is non-monotonic. It is noted that the total cross sections of all noble gases are non-monotonic functions of the relative velocity of interaction (Sharipov 2022, 2018a). As a result, since the relative velocity is proportional to temperature, many macroscopic characteristics, including the viscous and thermal slip coefficients, are non-monotonic functions of temperature.

5 Concluding remarks

The viscous and thermal velocity slip coefficients are computed by solving the corresponding half-space problems via the linearized Boltzmann equation, with ab initio potential, subject to Maxwell and Cercignani–Lampis boundary conditions. Complimentary results with hard sphere and Lennard–Jones potentials are provided for comparison purposes. Comparisons with data obtained via the linearized Shakhov model are also performed. The investigation includes five monatomic gases, namely He, Ne, Ar, Kr and Xe. The importance of quantum effects is considered by employing quantum and classical scattering theory to He, at temperatures from 1 K up to 10^4 K.

Extensive data of the computed viscous and thermal slip coefficients are tabulated. The reported results are considered of high accuracy and free from modelling approximations because they are based on the linearized Boltzmann equation, with ab initio potential. Furthermore, they have been benchmarked in various manners, such as fulfilment of reciprocity relation and comparisons with the associated slab geometry flows. The produced database is dense and covers the whole range of the accommodation coefficients. The results based on the ab initio potential and Cercignani–Lampis boundary conditions are provided for the first time in the literature. Furthermore, interpolation expressions of the viscous and thermal slip coefficients, based on HS potential, reproducing the tabulated data with deviations less than 0.4% are deduced. These expressions are easily implemented in the future computational and experimental works.

It is confirmed that the thermal slip coefficient depends, much more than the viscous slip coefficient, on the intermolecular potential and model kinetic equation. From the non-equilibrium thermodynamic point of view, this behaviour may be justified, at certain extend, considering that viscous slip coefficient is a direct phenomenon (Couette flow with an "infinite" distance between the stationary and moving plates), with pure momentum transfer, whilst the thermal slip coefficient is a cross phenomenon (thermal creep flow), with coupled momentum and energy transfer. Therefore, the latter one is more sensitive to imposed differences (potential, model equation, etc.). The variation of the viscous slip coefficient for various potentials is less than 3%, whilst of the thermal slip coefficient between the hard sphere and ab initio potentials is about 6% for He and increases, as the gas become heavier, reaching 15% for Xe. Also, the deviations of the data via the linearized Shakhov model with respect to the linearized Boltzmann equation are larger in the thermal, rather than in the viscous slip coefficient. Overall, the behaviour of the thermal and viscous slip coefficients in terms of the accommodation coefficients is qualitatively similar to the one of the Poiseuille and thermal creep flow rates respectively in the slip regime (Basdanis et al. 2022).

Concerning the deviations from the classical behaviour for light gases at low temperatures, it has been found that quantum effects are not important in the viscous slip coefficient, but they become important in the thermal slip coefficient. In the thermal slip coefficient of He, the differences between the classical and quantum approaches start to appear at $T_0 = 100$ K and reach 15% at $T_0 = 1$ K.

Since this is the first time that ab initio potentials are introduced into the linearized Boltzmann equation, it is worth to note that the involved computational effort is about the same as for the Lennard–Jones and significantly larger than for the hard sphere. However, ab initio potentials are based on first principles and do not contain any adjustable parameters, and therefore, in flow setups, where the hard sphere potential may produce erroneous results (e.g. mixtures), ab initio potential, instead of Lennard–Jones, should be employed.

Appendix 1: DCS based on ab initio potential with quantum and classical scattering

The AI potentials, employed in the present work, are cited in Cybulski and Toczyłowski (1999), Przybytek et al. (2010), Cencek et al. (2012), Hellmann et al. (2008), Patkowski and Szalewicz (2010), Jäger et al. (2009), Jäger et al. (2016), Jäger and Bich (2017), Haley and Cybulski (2003) and Hellmann et al. (2017) and have been obtained in the typical manner. They are calculated applying only the Coulomb interaction law between nuclei and all electrons of two atoms separated by some distance. It is assumed that electrons obey the Fermi–Dirac statistics with the Pauli's exclusion principle. Once the energy of two interaction atoms is calculated for several values of the separation, an interpolating formula for the potential is elaborated.

In the present work, the AI potential interpolation formulas are obtained from the literature and in Table 11, the exact reference with the associated equation for each gas, are cited. Particularly in the case of He, the retardation correction, given by Eq. (46) in Cencek et al. (2012), has been added to the potential (the supplementary material of Cencek et al. (2012) contains a code calculating the potential). Following the specification of the AI potential, the DCS is computed based on the quantum or classical theory following the methodologies described in Sharipov (2022), Sharipov (2018a) and Sharipov and Bertoldo (2009a) respectively.

Based on these methodologies, dense databases of the dimensional DCS $\sigma'(g', \chi)$ in terms of the dimensional relative speed g' and deflection angle χ have been created and are provided in the supplementary material for all involved gases in tabular form. Each value of DCS corresponds to a specific pair (g', χ). The characteristics of each of the six databases (five for quantum theory and one for classical theory) in the supplementary material are shown in Table 12, where the number of discrete values of g' and χ, along with their range, is specified. The DCS $\sigma'(g', \chi)$ and the relative speed g' may be converted to dimensionless form as $\sigma(g, \chi) = \sigma'(g', \chi)/d^2$ and $g = g'/v_0$ where the characteristic atomic size d of each gas is given in Table 13 (Sharipov and Benites 2021, 2020). In the quantum databases, the DCS has been calculated based on the spin n of the most representative isotope of each species, namely $n = 0$ for He, Ne, Ar, and Kr, whilst $n = 1/2$ for Xe. The data are available in the interval $(0, \pi/2]$ because they are symmetric with respect to $\chi = \pi/2$. In the classical database, the DCS is provided in the whole interval $(0, \pi)$.

In Figs. 8 and 9, some indicative comparisons between the DCS and TCS respectively of He for quantum and classical scattering theory, based on AI potential, are shown. Significant differences in the cross sections between quantum and classical theory are observed.

Appendix 2: Formulation of integral equations for viscosity and thermal conductivity

Following (Ivchenko et al. 2007; Ferziger and Kaper 1972), dimensionless viscosity μ and thermal conductivity κ are given by

$$\mu = \frac{1}{\sqrt{\pi}} \int_{-\infty}^{\infty} \int_{0}^{\infty} X^{(\mu)}(c_x, c_r) c_x c_r^3 \exp\left(-c_x^2 - c_r^2\right) dc_r dc_x. \quad (37)$$
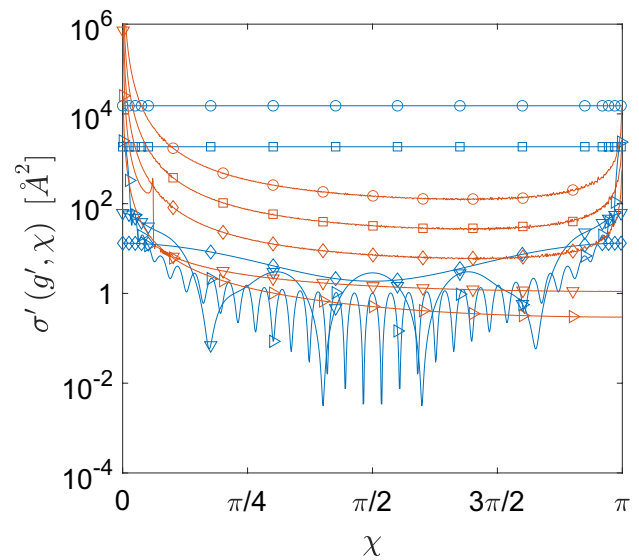

Fig. 8 Differential cross section $\sigma'(g', \chi)$ of He for quantum (blue lines) and classical (red lines) scattering based on AI potential vs the deflection angle χ at $g' = 1$ m/s (empty circle), $g' = 10$ m/s (empty square), $g' = 10^2$ m/s (empty diamond), $g' = 10^3$ m/s (empty inverted triangle) and $g' = 10^4$ m/s (empty rightward triangle)

$$\kappa = \frac{1}{\sqrt{\pi}} \int_{-\infty}^{\infty} \int_{0}^{\infty} X^{(\kappa)}(c_x, c_r) c_r^3 \left(c_x^2 + c_r^2 - \frac{5}{2}\right) \exp\left(-c_x^2 - c_r^2\right) dc_x dc_r, \quad (38)$$

respectively, where the functions $X^{(j)}(c_x, c_r)$, with $j = \kappa, \mu$, satisfy the integral equations

$$\tilde{L}\left[X^{(\mu)}(c_x, c_r)\right] + 2c_x c_r = 0, \quad (39)$$

$$\tilde{L}\left[X^{(\kappa)}(c_x, c_r)\right] + c_r\left(c^2 - \frac{5}{2}\right) = 0. \quad (40)$$

The integral equation (40) is not adequate for the computation of $X^{(\kappa)}$ and it is solved along with the additional constrain

$$\frac{1}{\sqrt{\pi}} \int_{-\infty}^{\infty} \int_{0}^{\infty} X^{(\kappa)}(c_x, c_r) \exp\left(-c_x^2 - c_r^2\right) c_r^3 dc_r dc_x = 0. \quad (41)$$

The linearized collision operators $\tilde{L}\left[X^{(j)}\right]$, $j = \kappa, \mu$, are written as

$$\tilde{L}\left[X^{(j)}\right] = \frac{1}{\pi^{3/2}} \int_{-\infty}^{\infty} \int_{0}^{\infty} \tilde{K}(c_x, c_r, \hat{c}_x, \hat{c}_r) \left[X^{(j)}(\hat{c}_x, \hat{c}_r) - X^{(j)}(c_x, c_r)\right] \exp\left(-\hat{c}_x^2 - \hat{c}_r^2\right) \hat{c}_r^2 d\hat{c}_r d\hat{c}_x, \quad (42)$$
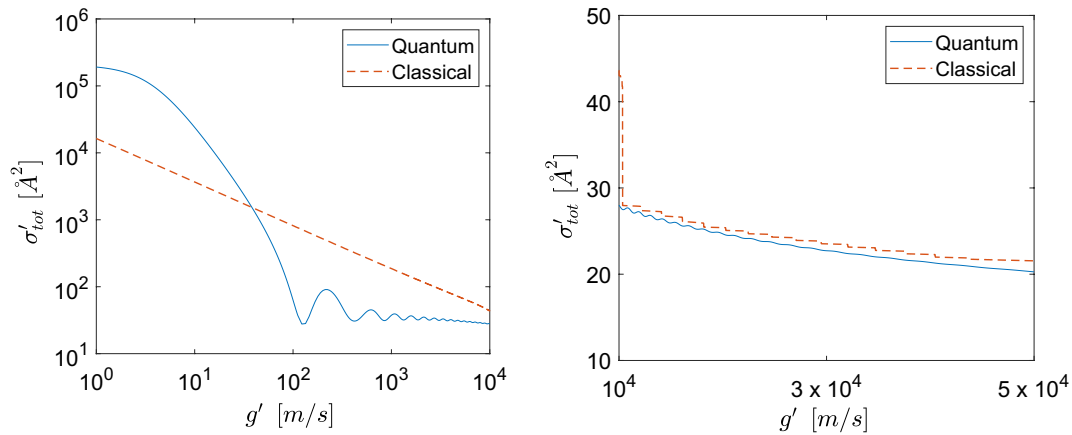
Fig. 9 Total cross section σ'_{tot} of He for quantum and classical scattering theory based on AI potential vs relative velocity g'

Table 11 AI potential interpolation formulas applied for each gas

Gas	He	Ne	Ar	Kr	Xe
Reference	Equation (60) in (Cencek et al. 2012)	Equation (4) in (Hellmann et al. 2008)	Equation (2) in (Patkowski and Szalewicz 2010)	Equation (8) in (Jäger et al. 2016)	Equation (6) in (Hellmann et al. 2017)

Table 12 Databases of DCS provided in supplementary material for the five gases

$\sigma'(g', \chi)$	Number of discrete g'	Range of discrete g'	Number of discrete χ
He (quantum)	11,000	$0.178 - 4.96 \times 10^5$	400
He (classical)	3181	$0.178 - 0.5416 \times 10^5$	999
Ne (quantum)	10,750	$0.1 - 10^5$	1000
Ar (quantum)	15,000	$0.3534 \times 10^{-3} - 0.1505 \times 10^7$	1000
Kr (quantum)	15,000	$0.01 - 0.1068686 \times 10^7$	1000
Xe (quantum)	13,800	$0.0101 - 0.62 \times 10^6$	1900

Table 13 Distance d[angstrom: Å] at which the AI potential is zero (Sharipov and Benites 2021, 2020)

He	Ne	Ar	Kr	Xe
2.641	2.761	3.358	3.581	3.902

where the kernel $\tilde{K}$ is given by Eq. (6) and the associated kernels (7) and (8) for the HS and AI potentials. Once the functions $X^{(j)}(c_x, c_r)$ are computed, the coefficients μ and κ are readily deduced from Eqs. (37) and (38) respectively, whilst the perturbed distribution functions $h^{(\mu)}(c_x, c_r)$ and $h^{(\kappa)}(c_x, c_r)$, employed in the reciprocity relation (21) are given by

$$h^{(j)}(c_x, c_r) = \frac{1}{2\mu} c_r X^{(j)}(c_x, c_r), \; j = \kappa, \mu. \tag{43}$$

Based on this analysis, tabulated data of μ and κ are provided in Sect. 4.1

Appendix 3: Formulation of the plane Couette, Poiseuille and thermal creep flows

For all three slab geometry problems, the dimensionless LBE is written as

$$c_x \frac{\partial Y_i(x, c_x, c_r)}{\partial x} = 2\mu\delta L(Y_i) + s_i(c_x, c_r), \tag{44}$$

where $-1/2 < x < 1/2$ and $i = C, P, T$ for the planar Couette, Poiseuille and thermal flows respectively. The linearized collision operators $L(Y_i)$ is given by Eqs. (5) and (6), with $\Psi_C = \Psi_P = \Psi_T = c_r$ and $Z_C = Z_P = Z_T = \cos\beta$. The source terms are:

$$s_C(c_x, c_r) = 0, \; s_P(c_x, c_r) = -c_r, \; s_T(c_x, c_r) = -c_r(c^2 - 5/2), \tag{45}$$

The diffuse boundary conditions at $x = \mp 1/2$ read as follows:

$$Y_C\left(\pm\frac{1}{2}, c_x, c_r\right) = \mp c_r, c_x \lessgtr 0, \tag{46}$$

$$Y_i\left(\pm\frac{1}{2}, c_x, c_r\right) = 0, c_x \lessgtr 0, i = P, T. \tag{47}$$

The dimensionless shear stress distribution $\Pi_C(x)$ in the Couette flow is obtained by

$$\Pi_C(x) = \frac{2}{\sqrt{\pi}} \int_{-\infty}^{\infty} \int_{0}^{\infty} \Upsilon_C\left(x, c_x, c_r\right) \exp\left(-c_x^2 - c_r^2\right) c_x c_r^2 \mathrm{d}c_r \mathrm{d}c_x, \tag{48}$$

and as it is well known it remains constant between the plates. The dimensionless flow rates G_P and G_T in the Poiseuille and thermal creep flows respectively, are obtained by

$$G_P = 2 \int_{-1/2}^{1/2} u_{y,P}(x)\mathrm{d}x \text{ and } G_T = 2 \int_{-1/2}^{1/2} u_{y,T}(x)\mathrm{d}x, \tag{49}$$

where the bulk velocity distributions $u_{y,P}(x)$ and $u_{y,T}(x)$ are computed according to Eq. (17).

For the slab geometry problems, the same numerical scheme as in the half-space problems is employed.

Declarations

Conflict of interest The authors declare no competing interests.

References

Basdanis T, Tatsios G, Valougeorgis D (2022) Gas-surface interaction in rarefied gas flows through long capillaries via the linearized Boltzmann equation with various boundary conditions. Vacuum 202:111152

Berg RF, Burton WC (2013) Noble gas viscosities at 25°C. Mol Phys 111(2):195–199

Bich E, Hellmann R, Vogel E (2008) Ab initio potential energy curve for the neon atom pair and thermophysical properties for the dilute neon gas. II. Thermophysical properties for low-density neon. Mol Phys 106(6):813–825

Bird GK (1994) Molecular gas dynamics and the direct simulation of gas flows, Oxford Engineering Science Series. Clarendon Press, Oxford

Breuer KS (2002) Chapter 9, Lubrication in MEMS. The MEMS handbook. CRC Press, Boca Raton

Cencek W, Przybytek M, Komasa J, Mehl JB, Jeziorski B, Szalewicz K (2012) Effects of adiabatic, relativistic, and quantum electrodynamics interactions on the pair potential and thermophysical properties of helium. J Chem Phys 136(22):224303

Cercignani C, Lorenzani S (2010) Variational derivation of second-order coefficients on the basis of the Boltzmann equation for hard-sphere molecules. Phys Fluids 22:062004

Cheetham P, Kim W, Kim CH, Graber L, Rodrigo H, Pamidi S (2016) Enhancement of dielectric strength of cryogenic gaseous helium by addition of small mol% hydrogen. IEEE Trans Appl Supercond 27(4):1–5

Colin S (2014) Single-phase gas flow in microchannels. Heat transfer and fluid flow in minichannels and microchannels. Elsevier, Oxford, pp 11–102

Cranmer M, Sanchez Gonzalez A, Battaglia P, Xu R, Cranmer K, Spergel D, Ho S (2020) Discovering symbolic models from deep learning with inductive biases. Adv Neural Inf Process Syst 33:17429–17442

Cybulski SM, Toczyłowski RR (1999) Ground state potential energy curves for He₂, Ne₂, Ar₂, He–Ne, He–Ar, and Ne–Ar: a coupled-cluster study. J Chem Phys 111(23):10520–10528

Ferziger JH, Kaper HG (1972) Mathematical theory of transport processes in gases. North-Holland Publishing Company, Amsterdam

Garcia RDM, Siewert CE (2010) Viscous-slip, thermal-slip, and temperature-jump coefficients based on the linearized Boltzmann equation (and five kinetic models) with the Cercignani–Lampis boundary condition. Eur J Mech B/fluids 29(3):181–191

Gibelli L (2012) Velocity slip coefficients based on the hard-sphere Boltzmann equation. Phys Fluids 24:022001

Graber L, Kim WJ, Cheetham P, Kim CH, Rodrigo H, Pamidi SV (2015) Dielectric properties of cryogenic gas mixtures containing helium, neon, and hydrogen. In: IOP conference series: materials science and engineering, vol 102(1). IOP Publishing, Bristol, p 012018

Haley TP, Cybulski SM (2003) Ground state potential energy curves for He–Kr, Ne–Kr, Ar–Kr, and Kr 2: Coupled-cluster calculations and comparison with experiment. J Chem Phys 119(11):5487–5496

Hart A, Gnanendran N (2009) Cryogenic CO_2 capture in natural gas. Energy Procedia 1(1):697–706

Hellmann R, Bich E, Vogel E (2008) Ab initio potential energy curve for the neon atom pair and thermophysical properties of the dilute neon gas. I. Neon–neon interatomic potential and vibrational spectra. Mol Phys 106(1):133–140

Hellmann R, Jäger B, Bich E (2017) State-of-the-art ab initio potential energy curve for the xenon atom pair and related spectroscopic and thermophysical properties. J Chem Phys 147(3):034304

Hirschfelder JO, Curtiss CF, Bird RB (1954) Molecular theory of gases and liquids. Wiley, New York

Ivchenko IN, Loyalka SK, Tompson RV (2007) Analytical methods for problems of molecular transport. Springer, Berlin

Jäger B, Bich E (2017) Thermophysical properties of krypton-helium gas mixtures from ab initio pair potentials. J Chem Phys 146(21):214302

Jäger B, Hellmann R, Bich E, Vogel E (2009) Ab initio pair potential energy curve for the argon atom pair and thermophysical properties of the dilute argon gas. I. Argon–argon interatomic potential and rovibrational spectra. Mol Phys 107(20):2181–2188

Jäger B, Hellmann R, Bich E, Vogel E (2016) State-of-the-art ab initio potential energy curve for the krypton atom pair and thermophysical properties of dilute krypton gas. J Chem Phys 144(11):114304

Johansson MV, Testa F, Perrier P, Vicente J, Bonnet JP, Moulin P, Graur I (2019) Determination of an effective pore dimension for microporous media. Int J Heat Mass Transf 142:118412

Jousten K (2016) Applications and scope of vacuum technology. In: Jousten K (ed) Handbook of vacuum technology. Wiley, Weinheim, pp 518–520

Kalinin V, Tada E, Millet F, Shatil N (2006) ITER cryogenic system. Fusion Eng Des 81:2589–2595

Kandlikar SG, Garimella S (2006) Heat transfer and fluid flow in minichannels and microchannels. Elsevier, Oxford

Le NT, White C, Reese JM, Myong RS (2012) Langmuir-Maxwell and Langmuir-Smoluchowski boundary conditions for thermal gas flow simulations in hypersonic aerodynamics. Int J Heat Mass Transf 55(19–20):5032–5043

Loyalka SK (1990) Slip and jump coefficients for rarefied gas flows: variational results for Lennard-Jones and n (r)-6 potentials. Phys A 163(3):813–821

Loyalka SK, Hickey KA (1990) The Kramers problem: velocity slip and defect for a hard sphere gas with arbitrary accommodation. Z Angew Math Phys ZAMP 41(2):245–253

Moghaddam RN, Jamiolahmady M (2016) Slip flow in porous media. Fuel 173:298–310

Mohan A, Tompson RV, Hickey KA, Loyalka SK (2008) Chapman-Enskog and Burnett solutions for a simple rigid-sphere gas: numerical solutions using a subtraction technique. J Quant Spectrosc Radiat Transf 109(5):741–751

Mozetič M et al (2014) Recent advances in vacuum sciences and applications. J Phys D Appl Phys 47(15):153001

Naris S, Vasileiadis N, Valougeorgis D, Hashad AS, Sabuga W (2018) Computation of the effective area and associated uncertainties of non-rotating piston gauges FPG and FRS. Metrologia 56(1):015004

Nguyen NN, Graur I, Perrier P, Lorenzani S (2020) Variational derivation of thermal slip coefficients on the basis of the Boltzmann equation for hard-sphere molecules and Cercignani–Lampis boundary conditions: comparison with experimental results. Phys Fluids 32(10):102011

Oh H, Hirscher M (2016) Quantum sieving for separation of hydrogen isotopes using MOFs. Eur J Inorg Chem 2016(27):4278–4289

Patkowski K, Szalewicz K (2010) Argon pair potential at basis set and excitation limits. J Chem Phys 133(9):094304

Pearce RJH, Antipenkov A, Bersier JL, Boussier B, Bryan S, Dremel M, Hughes S, Sekachev I, Worth L, Baylor L, Gardner W, Meitner S, Wikus P, Laesser R, Papastergiou S (2012) Gas species, their evolution and segregation through the ITER vacuum systems. Vacuum 86:1725–1730

Pearce RJ, Antipenkov A, Boussier B, Bryan S, Dremel M, Levesy B, Mayaux C, Wykes M (2013) The ITER divertor pumping system, design evolution, simplification and performance. Fusion Eng Des 88:809–813

Przybytek M, Cencek W, Komasa J, Łach G, Jeziorski B, Szalewicz K (2010) Relativistic and quantum electrodynamics effects in the helium pair potential. Phys Rev Lett 104(18):183003

Sharipov F (2006) Onsager-Casimir reciprocal relations based on the Boltzmann equation and gas-surface interaction: single gas. Phys Rev E 73(2):026110

Sharipov F (2011) Data on the velocity slip and temperature jump on a gas-solid interface. J Phys Chem Ref Data 40(2):023101

Sharipov F (2016) Rarefied gas dynamics: fundamentals for research and practice. Wiley, Oxford

Sharipov F (2018a) Modeling of transport phenomena in gases based on quantum scattering. Phys A 508:797–805

Sharipov F (2018b) Influence of quantum intermolecular interaction on internal flows of rarefied gases. Vacuum 156:146–153

Sharipov F (2022) Direct simulation Monte Carlo method based on ab initio potential: Recovery of transport coefficients of multicomponent mixtures of noble gases. Phys Fluids 34(9):097114

Sharipov F, Benites VJ (2020) Transport coefficients of multi-component mixtures of noble gases based on ab initio potentials: viscosity and thermal conductivity. Phys Fluids 32(7):077104

Sharipov F, Benites VJ (2021) Transport coefficients of isotopic mixtures of noble gases based on ab initio potentials. Phys Chem Chem Phys 23(31):16664–16674

Sharipov F, Bertoldo G (2009a) Numerical solution of the linearized Boltzmann equation for an arbitrary intermolecular potential. J Comput Phys 228(9):3345–3357

Sharipov F, Bertoldo G (2009b) Poiseuille flow and thermal creep based on the Boltzmann equation with the Lennard-Jones potential over a wide range of the Knudsen number. Phys Fluids 21(6):067101

Sharipov F, Dias C (2019) Temperature dependence of shock wave structure in helium and neon. Phys Fluids 31:037109

Sharipov F, Strapasson JL (2012a) Direct simulation Monte Carlo method for an arbitrary intermolecular potential. Phys Fluids 24(1):011703

Sharipov F, Strapasson JL (2012b) Ab initio simulation of transport phenomena in rarefied gases. Phys Rev E 86(3):031130

Sharipov F, Strapasson JL (2013) Benchmark problems for mixtures of rarefied gases. I. Couette Flow. Phys Fluids 25(2):027101

Shen C (2005) Rarefied gas dynamics: fundamentals, simulations and micro flows. Springer, Berlin

Siewert CE (2002) On computing the Chapman-Enskog functions for viscosity and heat transfer and the Burnett functions. J Quant Spectrosc Radiat Transf 74(6):789–796

Siewert CE (2003a) The linearized Boltzmann equation: concise and accurate solutions to basic flow problems. Z Angew Math Phys ZAMP 54(2):273–303

Siewert CE (2003b) Viscous-slip, thermal-slip, and temperature-jump coefficients as defined by the linearized Boltzmann equation and the Cercignani–Lampis boundary condition. Phys Fluids 15(6):1696–1701

Silva E, Rojas-Cardenas M, Deschamps CJ (2016) Experimental analysis of velocity slip at the wall for gas flows of nitrogen, R134a, and R600a through a metallic microtube. Int J Refrig 66:121–132

Sone Y, Ohwada T, Aoki K (1989) Numerical analysis of the shear and thermal creep flows of a rarefied gas over a plane wall on the basis of the linearized Boltzmann equation for hard-sphere molecules. Phys Fluids A 1(9):1588–1599

Strapasson JL, Sharipov F (2014) Ab initio simulation of heat transfer through a mixture of rarefied gases. Int J Heat Mass Transf 71:91–97

Tantos C, Naris S, Valougeorgis D (2016) Gas flow towards an adsorbing planar wall subject to partial gas-surface thermal accommodation. Vacuum 125:65–74

Vasileiadis N, Tatsios G, Misdanitis S, Valougeorgis D (2016) Modeling of complex gas distribution systems operating under any vacuum conditions: simulations of the ITER divertor pumping system. Fusion Eng Des 103:125–135

Vasileiadis N, Tatsios G, Valougeorgis D (2021) Pressure and temperature driven fully-developed rarefied gas flow in a channel with uniform injection/suction through its permeable walls. Vacuum 188:110155

Veijola T (2010) Gas damping in vibrating MEMS structures. In: Tilli M, Motooka T, Airaksinen V-M, Franssila S, Paulasto-Krckel M, Lindroos V (eds) Micro and nano technologies. William Andrew Publishing, Boston, pp 259–279

Verbovsek T, Setina Batic B, Setina J (2019) Investigation into the influence of surface conditions on the tube conductance for the molecular flow regime. Vacuum 161:150–156

Vogel E, Jäger B, Hellmann R, Bich E (2010) Ab initio pair potential energy curve for the argon atom pair and thermophysical properties for the dilute argon gas. II. Thermophysical properties for low-density argon. Mol Phys 108(24):3335–3352

Wang P, Su W, Wu L (2020) Thermal transpiration in molecular gas. Phys Fluids 32:082005

Wu L, Struchtrup H (2017) Assessment and development of the gas kinetic boundary condition for the Boltzmann equation. J Fluid Mech 823:511–537

Wu L, Liu H, Zhang Y, Reese JM (2015) Influence of intermolecular potentials on rarefied gas flows: fast spectral solutions of the Boltzmann equation. Phys Fluids 27:082002

Yamaguchi H, Perrier P, Ho MT, Méolans JG, Niimi T, Graur I (2016) Mass flow rate measurement of thermal creep flow from transitional to slip flow regime. J Fluid Mech 795:690–707

Zhang D, Miller FK, Pfotenhauer JM (2016) Solid deposition in the ITER cryogenic viscous compressor. Cryogenics 78:14–26

Zhang X, Ding S, Du F, Ji F, Xu Z, Liu J, Zhang Q, Zhou Y (2022) Investigation into gas lubrication performance of porous gas bearing considering velocity slip boundary condition. Friction 10(6):891–910

Zhu L, Wu L, Zhang Y, Sharipov F (2019) Ab initio calculation of rarefied flows of helium-neon mixture: classical vs quantum scatterings. Int J Heat Mass Transf 145:118765